Development of an ultra-stable seed laser operating in the HG33 Mode

Cheyanne Gruber[1,2]

Supervisor: Aaron Goodwin-Jones[1], Alexandr Bogomolov[1]

1. Université Catholique de Louvain, Pl. de l'Université 1, 1348 Ottignies-Louvain-la-Neuve, Belgium

2. American Military University, 111 W Congress St. Charles Town, West Virginia, United States of America

(Dated: July 20, 2025)

This letter details the methodology of, and my approach to, the reduction of thermal noise in terrestrial interferometric Gravitational Wave Detector (GWD) prototypes through the implementation of Higher-Order Mode (HOM) beam parameters. Keenly focused on the refinement of 6th order Hermite-Gaussian (HG) profiles, this experimental demonstration reports the design and commissioning of input optics, production of an ultra-stable laser source, and application of a Spatial Light Modulator (SLM) to overlay a quadratic phase profile effectively altering the fundamental Transverse ElectroMagnetic (TEM_{00}) mode.

Literature Review

1.1 Gravitational Wave Theory

The contrast of Einstein's Theory of General Relativity (GR) to the Newtonian formulation of Universal Gravitation reimagined gravity as a curvilinear effect of spacetime [1]. The tensor quality of a gravitational mass quadrupole moment allows for the precise calculation of quadrupolar radiation emissions under the consideration of conservation laws. These radiation emissions form characteristic quadrupolar patterns in spacetime that are studied to make informed astrophysical observations [2][3]. In the study of gravitational wave signals, multipole moments of a higher rank than the second time derivative of the quadrupole multipole moment (I=2) are considered sub-dominant modes. Therefore, we can express the spatial components for the second time derivative of a gravitational wave strain that is emitted from an evolving gravitational system by,

Equation 1

$$\begin{cases} \bar{h}^{\mu 0} = 0, \quad \mu = 0..3 \\ \bar{h}^{ik}(t,r) = \frac{2G}{c^4 r} \cdot \left[\frac{d^2}{dt^2}\, q^{ik}\left(t - \frac{r}{c}\right)\right] \end{cases}$$

wherein the first equation applies a gauge condition as component $\bar{h}^{\mu 0} = 0$ represents a trace-reversed metric perturbation tensor with a second index of 0, and $\mu = 0..3$ denotes a spacetime index with a range of values: [0, 1, 2, 3]. The equation structures the quadrupole formula representing the gravitational wave where $\bar{h}^{ik}$ denotes the spatial components of the indices of i and k. This is multiplied by time, t, and distance from the source, r, to represent the amplitude of the wave. This calculation demonstrates that the amplitude of the wave is proportional to the output of the prefactor containing 2 times the gravitational constant, G, divided by the speed of light in a vacuum, c^4, multiplied again by the distance from the source, r, multiplied by the result of the second time derivative, $\frac{d^2}{dt^2}$, times the retarded time, $(t - \frac{r}{c})$, of the mass quadrupole moment q^{ik}, respectively.

1.2 Gravitational Wave Interferometry

Interferometry leverages the diffraction of varying wavelengths along the Electromagnetic (EM) spectrum to induce observable interference patterns through the superposition of two or more coherent waves [4]. The resulting interplay of interferences from superposition, constructive and destructive, characterize interference fringes [5]. Rainer Weiss' conceptual adaptation of a Michelson Interferometer to form an L-shaped Interferometer applies this methodology to the detection of gravitational waves [6].

Global collaborations helped to realize Weiss' ideology of using distinctly spaced 'test masses' to measure distortions in spacetime. The successful development and operation of first- and second-generation ground-based gravitational wave interferometric observatories yielded the first irrefutable detection of gravitational waves on 14 September 2025 [3][7].

Presently, the sophisticated optical configurations of second-generation interferometric designs, such as dual Fabry-Pérot arm cavities, accentuate the laser phase shift by increasing the distance traveled within the optical resonator; thus, resulting in heightened sensitivity to the interference patterns upon output [8].

1.3 Gaussian Beams

Abiding by electromagnetism's fundamental laws, as described by Maxwell, the derivation of the Helmholtz equation is demonstrated through the manipulation of the vector wave equation. By substituting time dependance, these solutions allow observations of the mathematical product of a monochromatic wave's propagation [9][10]. Solutions of the paraxial wave equation, using the z-axis, project in the form of Gaussian amplitude and intensity profile functions [11]. The fundamental mode produced, TEM_{00}, demonstrates transverse components with zero nodes along two orthogonal axes [11].

Figure 1: Transverse ElectroMagnetic Mode 0,0 Profile

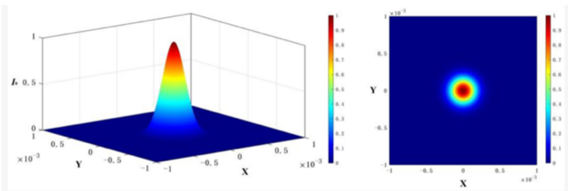

Image Credit: Ai, Y., Yan, Y., Yu, L., & Cheng, J. (2023).

1.4 Detector Noise Interferences

The amount of observable data that can be inferred by a gravitational wave event is dependent upon the signal-to-noise ratio of the GWD. The plethora of noises limit detections can be classified as either self-noise or external noise [12].

Self-noise corresponds to noise produced by detector and its subsystems. Examples of self-noises include quantum noise and suspension thermal noise [12][13][14][15]. Due to the typically stationary nature of these noises, their characteristics can be expressed in an amplitude spectral density plot [9][12].

External noises, such as seismic noise, are suppressed by the clever engineering of complex optomechanical structures [12][16]. Gravitational wave scientists and engineers assess the characteristic amplitude for propagation through the plant transfer function in order to calculate the residual noise [12][17].

Advanced data manipulation techniques, such as filtering and whitening, are used to recover gravitational wave signals from a spectral variance of noise sources [12].

1.5 Third-Generation Detectors

The multi-generational maturation of GWD sensitivity ranges is illustrated well in reports following the upgrade from initial to advanced LIGO and Virgo sites [18][19]. These improvements have yielded ranges of sensitivity 30 times lower at $f \sim 70\ Hz$ and have facilitated the detection of binary black hole mergers, with masses calculated to be 10 times that of our sun, by extending the Low Frequency (LF) sensitivity range from $f \sim 70\ Hz$ down to $f \sim 20\ Hz$ [18][19]. Many of these vital enhancements have been demonstrated through the implementation of innovative optical configurations and materials science [16][20]; however, the ongoing research and development of 3rd generation detectors such as the Einstein Telescope (ET) seek improvements by the further reduction of self-noise in interferometric designs [3][21][22].

Figure 2: The Einstein Telescope's High-Frequency Noise Budget

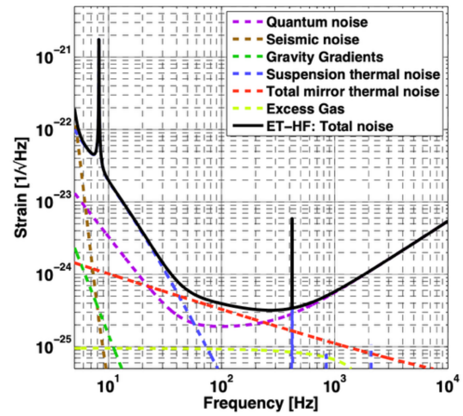

Image Credit: ET Steering Committee Editorial Team [20].

Classified as a self-noise, mirror thermal noise can be further categorized as Brownian and non-Brownian noises [13][14][15]. The proposal for ET is that the interferometer should be separated into two instruments. The first, is an LF interferometer with aimed sensitivity between $f \sim 3\ Hz$ to $f \sim 30\ Hz$ [3]. The second, is a High Frequency (HF) interferometer with a sensitivity range as depicted above. Also visible in Figure 3, the 'xylophone' configuration's HF total mirror thermal noise projections, specifically coating Brownian noises, impose limitations on the ET's sensitivity to strains in the mid-frequency band [3][21][22]. This self-noise begins to confine the strain noise floor at $f \sim 30\ Hz$ to $f \sim 200\ Hz$, and the greatest impact shown at $f \sim 100\ Hz$ with a strain noise contribution of $\sim 2 \cdot 10^{-25}\ 1/\sqrt{Hz}$.

1.6 Coating Brownian Noise

By applying observations of the kinetic molecular theory of matter, it has been reasoned that the intrinsic kinetic energy of any object, as expressed by its atomic motion, is measurable by the temperature of that object [21]. Coating Brownian noise manifests as an elastic response internal to thermal stresses of the mirror coating [24][25].

In tensorial form, the Fluctuation Dissipation Theorem (FDT) accounts for the vectoral displacement of optical components; however, the use of isotropic optical materials and amorphous coatings allows for the simplified use of a scalar FDT equation [13]. To mathematically support observations that explore the potential of mitigating thermal noise by means of Brownian averaging, we begin by using Levin's equation to define the PSD of coating Brownian noise [13].

Equation 2

$$S_x(f) = \frac{4k_BT}{\pi f}\phi U$$

Wherein, the displacement noise, $S_x(f)$, is characterized by the Boltzmann Constant, k_B, material's temperature, T, the frequency at which the noise is measured, f, the 'loss angle' or term of energy dissipation, ϕ, and the term for potential strain energy, U. In this application, the energy term is calculated by [24][25],

Equation 3

$$U = 2\pi \frac{1-\sigma^2}{Y}\int_0^\infty \tilde{I}(k)^2 dk$$

In which the Poisson ratio is given by σ, Young's modulus by Y, and the Hankel transform of the beam's intensity by $\tilde{I}(k)$ as derived from [15],

Equation 4

$$\tilde{I}(k) = \int_0^\infty I(r)J_0(kr)r\,dr$$

By narrowing the calculations of displacement noise to one dimension, we find that coating Brownian noise shares an inversely proportional relationship to the intensity profile of the beam upon the optical surface [14].

Equation 5

$$S_x \propto \frac{\int I^2(\vec{r})d^2\vec{r}}{[\int I^2(\vec{r})d^2\vec{r}]^2}$$

Experimental observations of HOMs have displayed their ability to distribute the intensity profile of the beam upon a larger portion of optical surfaces than the fundamental Gaussian mode, but prove less robust to mirror figure error in comparison to TEM_{00} [14][17].

1.7 Phase Noise

Following the establishment of Brownian noise's correlation to intensity distribution, we can then demonstrate that the relationship between the calculated displacement noise, S_χ, and phase noise, S_ϕ, along the laser's transmission axis is also directly proportional by,

Equation 6

$$\Delta\phi = \frac{4\pi}{\lambda}\,\Delta x$$

Wherein, the phase change, $\Delta\phi$, is equivalent to the Free Spectral Range (FSR) in units of radians divided by the wavelength or FSR in units of meters, $\frac{4\pi}{\lambda}$, multiplied by the optical displacement, Δx [26]. It is important to note that 4π is factored by changes in the total path length due to mirror displacement, $\Delta L = 2\Delta x$.

Methodology

2.1 Author's Note

The intended objective of the ETOPT project encompasses the research and development of a 10W ultra-pure, ultra-stable HG_{33} optical mode. In this research period, we will build an ultra-stable laser source to provide the framework for the generation of the seed laser. Following this evolution, the generation of the optical mode will be realized by use of a liquid-crystal display.

Three laser technologies were given consideration to include a Distributed Feedback (DFB), a Non-Planar Ring Oscillator (NPRO), and an External Cavity Diode Laser (ECDL). While NPRO's are the standard in the field of GW instrumentation, their precision would be negated by the added noise of the SLM's display, and the high noise emitted by DFB lasers at MHz frequencies make them unsuitable for 3rd generation prototypes [20]. The determination to design an ECDL was made due to its competitive performance and high level of customizability which is useful for SLM generated noise suppression [20]. See section 2.2 for a further description of the ECDL and its operating principle.

The methodology of pursing the use of an SLM to structure the phase profile allows for flexibility in the production of the desired optical mode, HG_{33}, where mode mismatch to the phase plate can be digitally compensated; thus, a display compatible with high optical intensities was purchased [27]. To achieve the ideal suppression of unwanted characteristics, our display limits the maximum phase shift to 2.4π at 1064nm with a phase flicker of ~0.05% [28]. This device has been temperature stabilized to optimize operating conditions, but the remaining phase ripple would require active stabilization. See section 2.3 for a further description of the SLM and its operating principle.

2.2 External Cavity Diode Laser

Focused on wavelengths in the near infrared (NIR), I constructed a tunable, research-grade ECDL, Peltier controller, and instrument control system with the assistance of Alexandr Bogomolov[1].

[1] Alexandr.Bogomolov@uclouvain.be

Using Doret's calculations [29], the ECDL modeled a modified Littrow configuration featuring a Plane Holographic Reflection Grating with 1800 grooves/mm. To ensure proper collimation and wavefront flatness of the Gaussian output, the grating equation was used.

Equation 7

$$Sin(a) = \frac{m\lambda}{2d} \qquad Sin(73.26) \approx \frac{(1)(1064)}{2(555.56)}$$

Wherein, the product of the incidence angle, *a*, and *Sin* function is proportional to the product of the diffraction order, *m,* and the operating wavelength, λ, divided by the doubled count of spacing between vicinal grooves [29].

Figure 4: Laser Diode Mounting

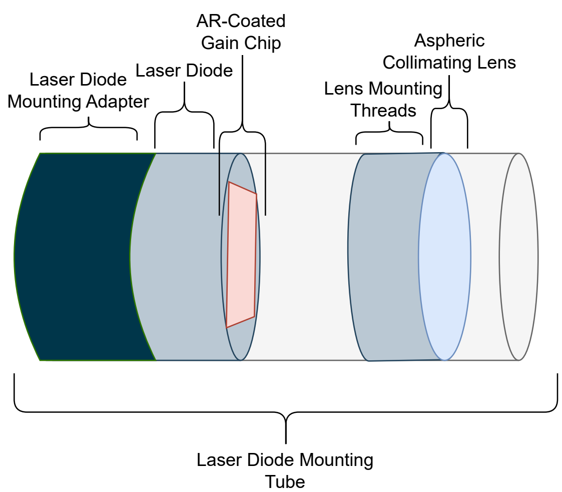

Figure 5: Top View of Littrow Configuration

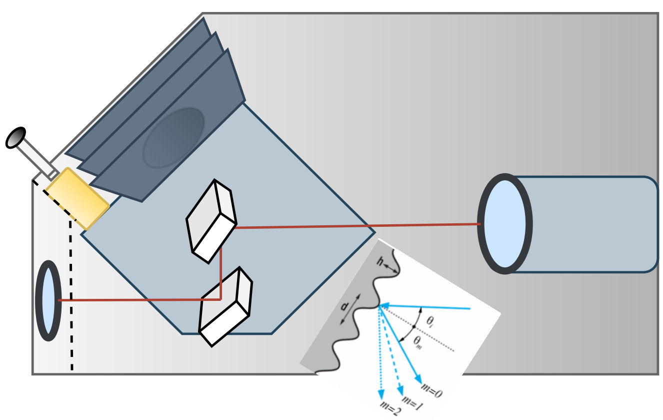

Credit for the inlaid grating angle diagram: *Thorlabs, [30].*

To begin characterizing the ECDL output, I calculated the Numerical Aperture (NA) of the laser diode along both the parallel and perpendicular axes and approximated the beam radius of each axis following the collimating lens by,

Equation 8

$$NA \parallel : Sin\left(\frac{10º}{2}\right) \approx 0.087 \quad NA \perp : Sin\left(\frac{24º}{2}\right) \approx 0.208$$

$$\parallel : 2(4.5mm) \cdot \tan\left(\frac{10º}{2}\right) \approx 0.395mm\ Radius$$

$$\perp : 2(4.5mm) \cdot \tan\left(\frac{24º}{2}\right) \approx 0.955mm\ Radius$$

Wherein, the manufacturer's data sheet for the laser diode, EYP-RWE-1060-10020-1500-SOT02-000 [31], provided the divergence angles of 10º and 24º while the manufacturer's data sheet for the collimating lens, C230TMD-C [32], provided the focal length of 4.5mm [33].

Due to the rectangular shape of the active area on the laser diode's gain chip, rotational adjustments to the lens' positioning were necessary to minimize the beam divergence and astigmatism. Fine adjustments to the distance positioning of the kinematic stage were also made to position the beam waist along the z-axis. The intensity peak of our Gaussian profile output was stabilized at 53.3 mW with a photodiode (PD) reading of 103mW at 130 mA of power applied by the instrument control system and a controlled temperature of 27º.

Figure 6:

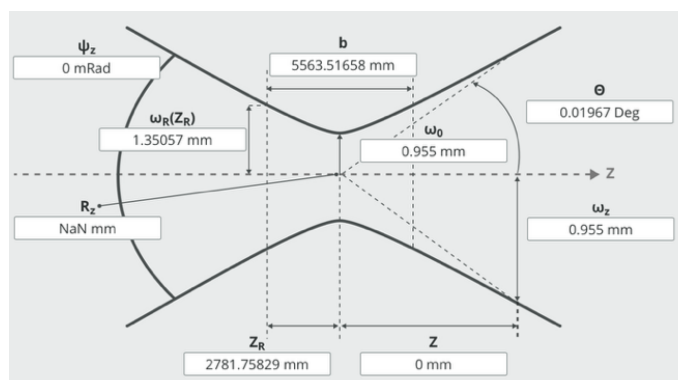

Image Note: This 3D-Optix simulation represents the parallel properties of the ECDL's ellipticity following colimitation [34].

Figure 7

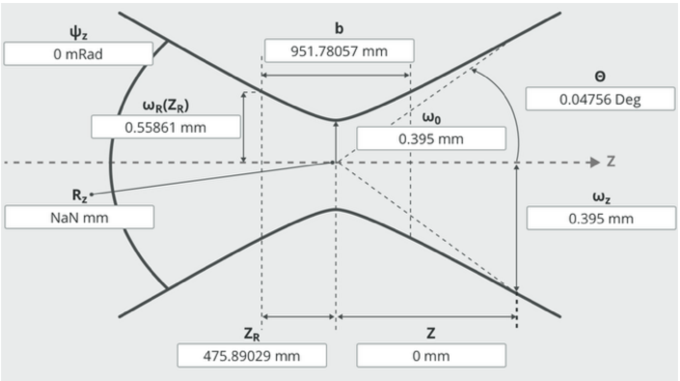

Image Note: 3D-Optix simulation representing the perpendicular properties of the ECDL's ellipticity following colimitation [34].

To properly define the operating wavelength, we coupled to optical fiber [35]. By using single-mode optical fiber as a spatial filter, the free-space TEM_{00} mode's imperfect Gaussian profile is translated into a Linearly Polarized, LP_{01}, spatial pattern. As depicted in Figure 8, the beam's qualities were monitored using a wavelength meter as we tuned the laser output wavelength by manually driving the Piezoelectric Transducer (PZT) driver circuit [35].

Figure 8

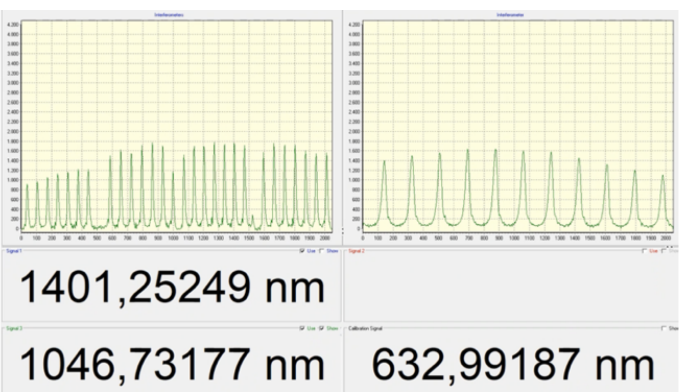

Image Note: The green signal charted and numerical measurement in the lower left depicts the ECDL. Values indicated represent process rather than finality.

Following the characterization of our laser, a directional mirror was mounted to the breadboard intersecting the beam path prior to the fiber collimator. This strategic step returns our defined, ultra-stable laser to free-space while maintaining the option to use the coupled optical fiber for driving the PZT.

2.3 Spatial Light Modulation

Our optical configuration featured a phase-only SLM driver with the active area positioned in a horizontal orientation and aligned to the transmission axis of the TEM_{00} beam [36]. The active area of the SLM is composed in layers consisting of an Anti-Reflection (AR) coating on a transparent glass substrate, a transparent electrode layer of Indium-Tin-Oxide (ITO), a polymer alignment layer, a layer of Vertical Aligned Nematic (VAN) liquid crystals, another polymer alignment layer, the dielectric mirror array situated with an 8.0 μm pixel pitch, and the Complementary Metal-Oxide-Semiconductor (CMOS) silicon chip backplane [27]. By applying a voltage between the ITO node and the CMOS chip, the alignment of the liquid crystals can be tuned, thus tuning the phase of the light passing through the voxel.

Figure 9: SLM Active Area

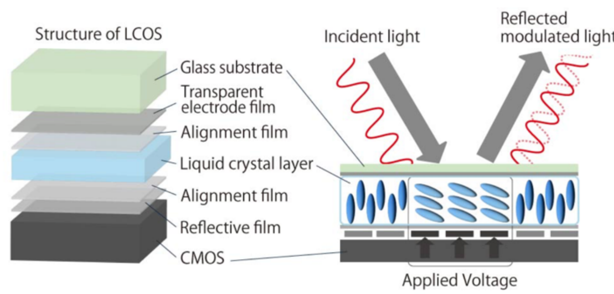

Image Credit: Santec, [37].

In order to effectively alter the phase profile of our laser upon output, several phase profiles were constructed using the SLM's provided Pattern Generator software [27]. The phase hologram applied is translated into an analog voltage map through the CMOS silicon chip providing the pixelated dielectric mirror array the direction of movement that shapes that VAN liquid crystals; thus, by illumination of the Liquid Crystal on Silicon (LCoS) microdisplay, the phase profile is imprinted upon the beam [27].

The desired quadratic phase profile generated in our experiments, HG_{33}, has a spatial mode of higher transverse order achieved by the multiplication of the Gaussian function and the third-order Hermite polynomial in the *x*- and *y*-directions by [16][38],

Equation 9

$$E_{33}(x,y,z) = E_0 \frac{w_0}{w(z)}$$

$$\cdot\ H_3\left(\sqrt{2}\frac{x}{w(z)}\right) e^{-\frac{x^2}{w(z)^2}} \cdot\ H_3\left(\sqrt{2}\frac{y}{w(z)}\right) e^{-\frac{y^2}{w(z)^2}}$$

$$\cdot\ e^{-i\left[kz-\left(1+3+3\arctan\left(\frac{z}{z_R}\right)\right)+\frac{k(x^2+y^2)}{2R(z)}\right]}$$

wherein $E_{33}(x, y, z)$ represents the electrical field of the beam at a 3rd dimension in space with the defining coordinates of (x, y, z), and the order of the HG mode with subscripts n and m that denote integers (0,1,2) in the x- and y- directions. E_0 serves as the amplitude constant or maximum strength at the central beam waist of the given electrical field in the mode of $(n = 3, m = 3)$. The scale of the beam's amplitude along the z-axis is given by $\frac{w_0}{w(z)}$, in which the beam waist, w_0, is the minimum radius of the beam's focal point divided by the beam radius from z to the beam waist, $w(z)$. This is multiplied by the Hermite polynomial in the n^{th} order mode to the power of the Gaussian function denoting the amplitude profile in the x-direction, multiplied by the Hermite polynomial in the m^{th} order mode to the power of the Gaussian function denoting the amplitude profile in the y-direction. Lastly, this is multiplied by product of the exponential term that defines the phase of the electrical field, wherein $k = \frac{2\pi}{\lambda}$ represents the planar phase in the z-direction, minus the Gouy phase shift, as determined by propagation distance, z, the Rayleigh range, z_R, and the mode orders $(n = 3, m = 3)$, plus the term for the curved wavefront phase, $\frac{k(x^2+y^2)}{2R(z)}$.

By using a ThorLabs DCC1545M sensor (Micron MT9M001) in the first diffraction order of the SLM's reflection I was able to record images of the HOMs generated [39]. Subsequent modal decomposition analyses of the recorded images were then performed.

2.4 Validation of the Mode Decomposition

We used a python script to prepares the images and conduct the modal decomposition analysis. Preparations include converting images to greyscale and applying a Fourier notch filter to convert the frequency spectrum using a Fourier Fast Transform (FFT) in order to remove prominent diagonal interference fringes of the high-frequency periodic noise exposure.

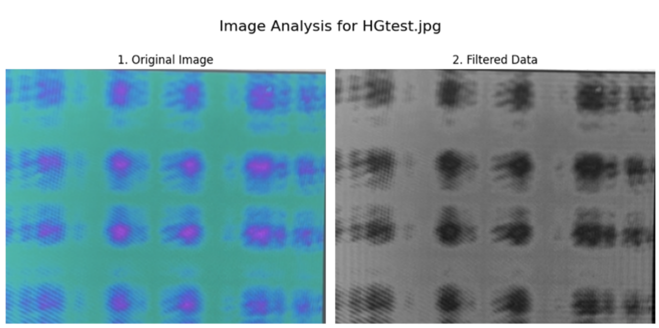

Image Note: Example modal decomposition analysis visual result

2.5 Producing Pure Optical Modes

Various approaches were explored to optimize the diffracted HG_{33} mode's clarity by adjusting the CGH and optical configuration. The mode trials imaged below reflect the investigated use of a blazed grating, manipulation of the beam's diameter, manipulation of the laser's polarization state, and tuning parameters within the pattern generator software to implement control over the beam's interaction with the SLM.

Figure 10: HG_{33} Mode Trials

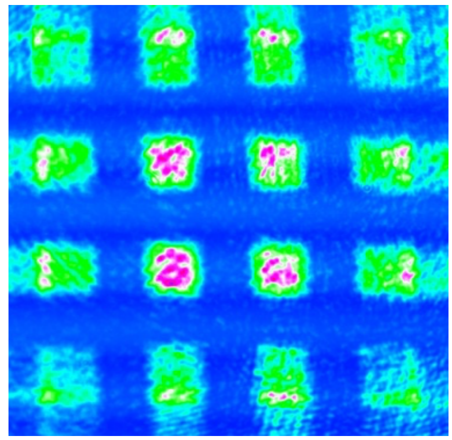

Image Note: Modal decomposition analysis results indicate this image has an HG_{33} mode purity of 59.1%, with primary contaminants of HG_{32} (8.8%), HG_{23} (8.1%), HG_{43} (5.2%) and 40.9% total power in other modes.

Figure 11: HG_{33} Mode Trials

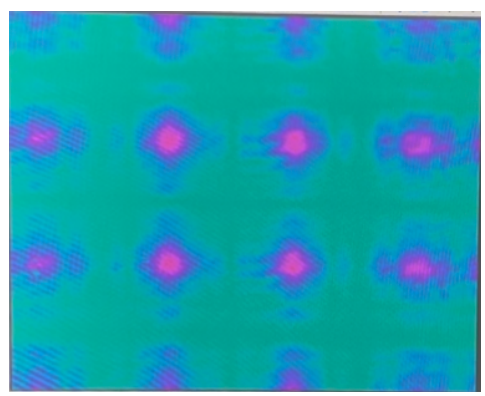

Image Note: Modal decomposition analysis results indicate this image has an HG_{33} mode purity of 70.8%, with primary contaminants of HG_{32} (6.5%), HG_{23} (6.1%), HG_{43} (4.3%) and 29.2% total power in other modes.

Figure 12: HG_{33} Mode Trials

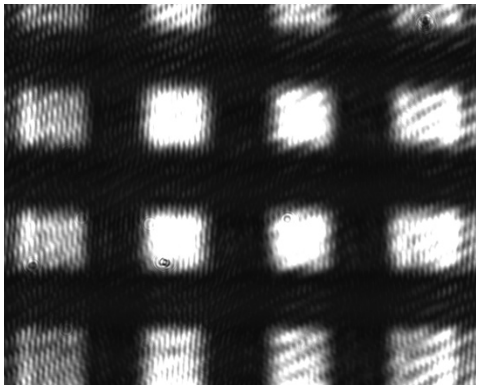

Image Note: Modal decomposition analysis results indicate this image has an HG_{33} mode purity of 83.9%, with primary contaminants of HG_{32} (3.8%), HG_{23} (3.2%), HG_{44} (2.1%) and 16.1% total power in other modes.

Figure 13: HG_{33} Mode Trials

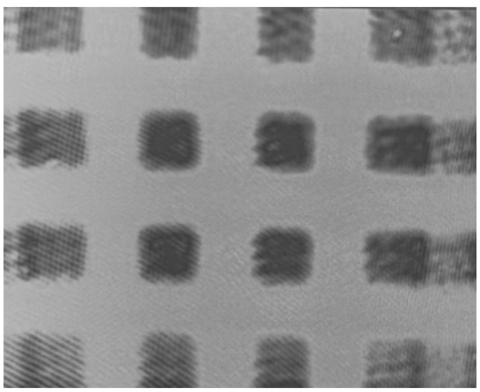

Image Note: Modal decomposition analysis results indicate this image has an HG_{33} mode purity of 92.1%, with primary contaminants of HG_{32} (1.9%), HG_{23} (1.5%), HG_{00} (1.2%) and 7.9% total power in other modes.

2.6 Optical Cavity

The intentional design of a V-shaped cavity introduces astigmatism through the bias angle of the folding mirror to accentuate the resonance of HG modes [40]. This technique differentiates the effective focal lengths of the tangential, *x-*, and sagittal, *y-*, planes of the n^{th} and m^{th} orders of the HG_{33} mode which proves advantageous when attempting to stabilize the HOM in an optical laser resonator [40]. Distinctly considering the factors of the total phase in the resonance condition, propagation phase and Gouy phase shift [40].

Measurements of the Invar bar's dimensions and specifications of the mirrors to be installed in each position allowed me to quantify the ABCD matrices to include the round-trip mode separation and resonance phase for the HG_{33} mode in the V-shaped cavity. A Finesse simulation was used to validate these calculations which allow us to remove the probability of other HOMs resonating at our operating frequency [41].

In order to establish a stable cavity eigenmode, with selective resonance in the HG_{33} mode, alignment procedures were conducted. The use of two irises helped to define a propagation vector that is coplanar with the principal plane of the optical table. This axis serves as the reference position for the mounting of the V-shaped cavity in which the input mirror and one end mirror are oriented to intercept the incident beam nominally. The folding mirror is then precisely installed at a bias angle to introduce controlled astigmatism.

Once all components were placed, a series of iterative pitch and yaw adjustments were made to the end mirror to appropriately direct the intracavity beam to a point of retro-reflection. This condition is ascertained when the beam exiting the input mirror is both collinear to and spatially coincident with the incident beam; thus, achieving clear execution of a round trip in the optical resonator.

Figure 14: Finesse Cavity Simulation

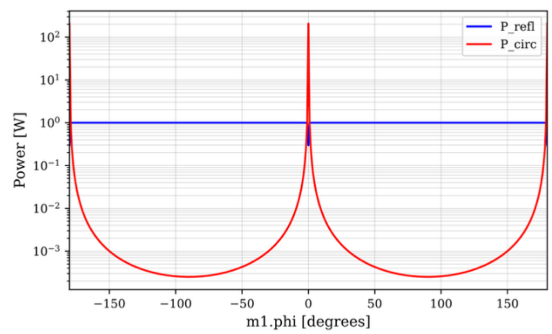

Image Credit: Finesse, [41].

Figure 15: Optical Configuration

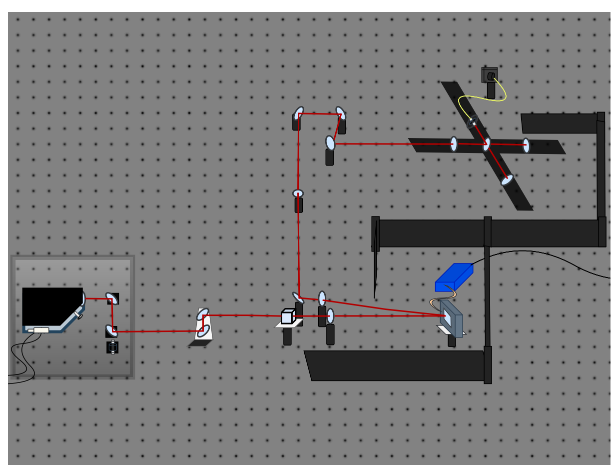

Conclusion

This research period yielded the successful construction and commissioning of an External Cavity Diode Laser for ongoing experimentation. This seed laser's stable operation was achieved through collimating, characterization, and tuning procedures at both 1070 nm and 1030 nm. The latter of which wavelengths was chosen for experimental purposes due to cavity compatibility.

A Spatial Light Modulator was leveraged to transform the fundamental Gaussian beam into the higher-order HG_{33} mode. To optimize the purity of the desired spatial and phase profile, several approaches were investigated. The results reflect an obtained mode purity of 92.1%.

The successful generation of a high-purity HG_{33} mode using the SLM and ECDL supports future aims of reducing the power spectral density of thermal noise interferences in ultra-stable interferometry; however, the initial modal decomposition analyses ran indicate that the beam will require significant spatial filtering before implementation in a gravitational wave detector prototype under the ETOPT project.

The design and construction of the V-shaped optical cavity intends to promote the resonance of pure higher-order modes. While substantial progress was made in aligning the cavity, scans verifying the filtering performance and confirm the mode decomposition measurements were not completed. These future characterizations will be undertaken by a PhD student's continuation of my research.

ACKNOWLEDGMENTS

The following experimental observations were coordinated by the University of Florida, supported by National Science Foundation award PHY-2348913, and hosted at Univerité Cathloiqué de Louvain from 1 June 2025 to 29 July 2025. Under the supervision of Dr. Aaron Goodwin-Jones, these efforts are considered for testing at the ETOPT facility following experimentation at the Centre for Cosmology, Particle Physics, and Phenomenology (CP3) and occupying laboratory space in the Nanoscopic Physics Division (NAPS) to conduct associated research.

I would like to thank the coordinating members from The University of Florida for the opportunity to participate in this IREU, and the collaborative efforts made by the UClouvain, CP3, and NAPS personnel to facilitate this research. I would also like to gratefully acknowledge the Region-Waloon (RW) for the financial support under the convention 2410083 "ETOPT" project, Win4Project program.

Additionally, I would like to formally thank Aaron Goodwin-Jones for his mentorship, Alexandr Bogomolov for his expertise, Clément Lauzin for his challenging insights, Giacomo Bruno for his time, and Ricardo Cabrita for sharing his experience.

This report has been allocated #304047 in the UCLouvain DIAL repository. https://dial.uclouvain.be/pr/boreal/object/boreal:304047

[1] A. Einstein, "The Foundation of the General Theory of Relativity," *Annalen der Physik*, vol. 49, no. 7, pp. 769–822, 1916. [Online]. Available: https://ia801204.us.archive.org/5/items/the-foundation-of-the-general-theory-of-relativity/The%20Foundation%20of%20the%20General%20Theory%20of%20Relativity.pdf

[2] "Chapter 14: The Quadrupole Formalism," INFN Roma1, 2021. [Online]. Available: https://www.roma1.infn.it/teongrav/VALERIA/TEACHING/quadrupolo.pdf

[3] ET Steering Committee Editorial Team, Ed., "Design Report Update 2020 for the Einstein Telescope," Gravitational Wave International Committee, ET-0007B-20, 2020. [Online]. Available: https://gwic.ligo.org/3Gsubcomm/docs/ET-0007B-20_ETDesignReportUpdate2020.pdf

[4] "What is an Interferometer?," *LIGO Lab | Caltech*. [Online]. Available: https://www.ligo.caltech.edu/page/what-is-interferometer

[5] C. Baird, "When does a light beam have only a single frequency?," *Science Questions With Surprising Answers*, May 8, 2014. [Online]. Available: https://www.wtamu.edu/~cbaird/sq/2014/05/08/when-does-a-light-beam-have-only-a-single-frequency/

[6] "Rainer Weiss life story," *The Kavli Prize*. [Online]. Available: https://www.kavliprize.org/rainer-weiss-autobiography

[7] B. P. Abbott *et al.*, "Properties of the Binary Black Hole Merger GW150914," *Phys. Rev. Lett.*, vol. 116, no. 24, Art. no. 241102, Jun. 2016, doi: 10.1103/physrevlett.116.241102.

[8] "LIGO's Interferometer," *LIGO Lab | Caltech*. [Online]. Available: https://www.ligo.caltech.edu/page/ligos-ifo?highlight=interferometer

[9] N. Christensen and F. Bondu, "LIGO S6 detector characterization studies," *Class. Quantum Gravity*, vol. 27, no. 19, Art. no. 194010, 2010, doi: 10.1088/0264-9381/27/19/194010.
[10] A. E. Siegman, *Lasers*. Sausalito, CA: University Science Books, 1986. [Online]. Available: https://archive.org/details/lasers0000anth/page/n7/mode/2up
[11] Y. Ai, Y. Yan, L. Yu, and J. Cheng, "The Analysis of Energy Distribution Characteristics of Molten Pool in Welding of Aluminum Alloy with Oscillating Laser," *Sustainability*, vol. 15, no. 8, p. 6868, Apr. 2023, doi: 10.3390/su15086868.
[12] B. P. Abbott *et al.*, "A guide to LIGO–Virgo detector noise and extraction of transient gravitational-wave signals," *Class. Quantum Gravity*, vol. 37, no. 5, Art. no. 055002, Feb. 2020, doi: 10.1088/1361-6382/ab685e.
[13] Y. Levin, "Internal thermal noise in the LIGO test masses: A direct approach," *Phys. Rev. D*, vol. 57, no. 2, pp. 659–663, Jan. 1998, doi: 10.1103/physrevd.57.659.
[14] T. Hong, "Brownian thermal noise in interferometric gravitational wave detectors and single photon optomechanics," Ph.D. dissertation, California Inst. Technol., Pasadena, CA, 2013. [Online]. Available: https://thesis.library.caltech.edu/7178/3/Thesis_TingHong_2013.pdf
[15] J. Y. Vinet, "On special optical modes and thermal issues in advanced gravitational wave interferometric detectors," *Living Rev. Relativ.*, vol. 12, no. 5, 2009, doi: 10.12942/lrr-2009-5.
[16] C. Bond, D. Brown, A. Freise, and K. A. Strain, "Interferometer techniques for gravitational-wave detection," *Living Rev. Relativ.*, vol. 19, no. 1, Art. no. 3, Dec. 2016, doi: 10.1007/s41114-016-0002-8.
[17] A. W. Jones and A. Freise, "Increased sensitivity of higher-order laser beams to mode mismatches," *Opt. Lett.*, vol. 45, no. 20, pp. 5876–5878, Oct. 2020. [Online]. Available: https://opg.optica.org/ol/abstract.cfm?URI=ol-45-20-5876
[18] Z. Chen *et al.*, "Quantum Sensing with Squeezed-Light-Enhanced Atom Interferometry," arXiv preprint arXiv:2411.14607, 2024.
[19] The LIGO Scientific Collaboration, "Enhancing the sensitivity of the LIGO gravitational wave detector by using squeezed states of light," LIGO, Tech. Rep. LIGO-P1200041-v19, 2013.
[20] Z. J. Holmes, "2 μm Lasers for Cryogenic-Silicon Gravitational Wave Detectors," Ph.D. thesis, The Univ. of Adelaide, Adelaide, SA, Australia, 2025. [Online]. Available: https://digital.library.adelaide.edu.au/items/6587a1c0-bc15-4a94-9bf9-bc12f5793785
[21] B. Sathyaprakash *et al.*, "Scientific objectives of Einstein Telescope," *Class. Quantum Gravity*, vol. 29, no. 12, Art. no. 124013, 2012, doi: 10.1088/0264-9381/29/12/124013.
[22] ET Science Team, Ed., "Einstein Gravitational Wave Telescope Conceptual Design Study," European Gravitational Observatory, Cascina, Italy, Rep. ET-0106C-10, 2011. [Online]. Available: https://apps.et-gw.eu/tds/?r=8709
[23] D. V. Schroeder, *An Introduction to Thermal Physics*. Oxford, UK: Oxford University Press, 2021, doi: 10.1093/oso/9780192895547.001.0001.
[24] P. Fulda, "Precision Interferometry in a New Shape: Higher-Order Laguerre-Gauss Modes for Gravitational Wave Detection," Ph.D. dissertation, Univ. of Birmingham, Birmingham, U.K., 2012. [Online]. Available: https://gwic.ligo.org/assets/docs/theses/fulda-thesis.pdf
[25] P. Fulda, "Coherent Waveburst Analysis of Gravitational Wave Data," Ph.D. dissertation, Albert Einstein Inst., Potsdam, Germany, 2012. [Online]. Available: https://gwic.ligo.org/assets/docs/theses/fulda-thesis.pdf
[26] M. Born and E. Wolf, *Principles of Optics*, 7th ed. Cambridge, U.K.: Cambridge University Press, 1999.
[27] "ERIS-1.1 Phase Only Spatial Light Modulator," *HOLOEYE Photonics AG*, Mar. 20, 2025. [Online]. Available: https://holoeye.com/products/spatial-light-modulators/eris-phase-only-spatial-light-modulator/
[28] A. Goodwin-Jones, "Selection Document - UCLouvain Spatial Light Modulator," Institut de Recherche en Mathématique et Physique, UCLouvain, Louvain-la-Neuve, Belgium, Rep. 2025/IRMP/GW/SLM, Apr. 28, 2025.
[29] S. C. Doret, "Simple, low-noise piezo driver with feed-forward for broad tuning of external cavity diode lasers," *Rev. Sci. Instrum.*, vol. 89, no. 2, Art. no. 023106, Feb. 2018, doi: 10.1063/1.5009643.
[30] "Diffraction gratings tutorial," *Thorlabs*. [Online]. Available: https://www.thorlabs.com/newgrouppage9.cfm?objectgroup_id=9026
[31] eagleyard Photonics GmbH, "AR coated Fabry-Perot Laser," Datasheet EYP-RWE-1060-10020-1500-SOT02-0000, 2017. [Online]. Available: https://www.toptica-eagleyard.com/wp-content/uploads/data_sheets/EYP-RWE-1060-10020-1500-SOT02-0000.pdf
[32] Thorlabs, "MOUNTED 0.55 NA ASPHERIC LENS, f=4.5 mm, DW=780 nm, C COATED," Drawing C230TMD-C. [Online]. Available: https://www.thorlabs.com/drawings/2a36e8098b4df35a-21070F7E-C77C-E8DF-ED5552C6A3D14C9F/C230TMD-C-AutoCADPDF.pdf
[33] B. E. A. Saleh and M. C. Teich, *Fundamentals of Photonics*, 3rd ed. Hoboken, NJ: Wiley, 2019.
[34] 3DOptix, *3DOptix*, 2025. [Online software]. Available: https://www.3doptix.com/
[35] C. Bragard, "Construction, characterisation and frequency stabilisation of an External Cavity Diode Laser for future high-precision and high-power studies," M.S. thesis, École de Physique, UCLouvain, Louvain-la-Neuve, Belgium, 2025.
[36] D. A. Steck, "Classical and Modern Optics," University of Oregon, 2008. [Online]. Available: http://www.nadirpoint.de/Physik_Lit_PDF/61.pdf
[37] "What is a Spatial Light Modulator?," *Santec*. [Online]. Available: https://www.santec.com/en/products/components/slm/SLMblog1/
[38] R. Paschotta, "Hermite-Gaussian modes," *RP Photonics Encyclopedia*, Apr. 5, 2025. [Online]. Available: https://www.rp-photonics.com/hermite_gaussian_modes.html
[39] Thorlabs, "DCC1545M - 1.3 Megapixel, Monochrome, High-Speed, CMOS Camera," Drawing DCC1545M. [Online]. Available: https://www.thorlabs.com/drawings/6d301ae

17648705-5350FACF-CED4-EB21-6D4C3CE3B48518C3/DCC1545M-AutoCADPDF.pdf.
[40] L. Tao, A. C. Green, and P. Fulda, "Higher-order Hermite-Gauss modes as a robust flat beam in interferometric gravitational wave detectors," *Phys. Rev. D*, vol. 102, no. 12, p. 122002, Dec. 2020, doi: 10.1103/PhysRevD.102.122002.
[41] "Finesse 3." [Online]. Available: https://finesse.ifosim.org/.